Computer Modeling in
Engineering & Sciences

Tech Science Press

https://doi.org/10.32604/cmes.2026.075681

ARTICLE

Nonlinear Dynamic Large Deformation Analysis of Hyperelastic Beams Based on the Gent Constitutive Model

Nasser Firouzi*

Institute of Structural Mechanics, Bauhaus-University Weimar, Weimar, Germany

*Corresponding Author: Nasser Firouzi. Email: nasser.firouzi92@gmail.com

Received: 06 November 2025; Accepted: 23 February 2026; Published: 27 May 2026

ABSTRACT: This study investigates finite transient deformations in hyperelastic beam structures based on the Gent material model. To enable its application within beam formulations, the Gent model is expressed in a linearized form. A five-parameter beam element, incorporating two displacement variables, two difference parameters, and one thickness parameter, is adopted. The nonlinear dynamic response is solved using the implicit Newmark method, allowing efficient analysis of beams subjected to complex loading and boundary conditions. The results show that the proposed approach accurately captures the response of geometrically nonlinear beams and reproduces the behavior of neo-Hookean hyperelastic beams when the extensibility parameter of the Gent model approaches very large values. As the extensibility parameter decreases, the influence of chain extensibility becomes increasingly pronounced. This effect is particularly relevant for applications involving rubber and soft-robotic beams, bio-inspired flexible structures, and elastomeric beams subjected to large-strain vibrations, impact, and other transient loading conditions.

KEYWORDS: Transient response; beam structures; hyperelasticity; gent model; newmark method

1 Introduction

The study of large deformations in hyperelastic beams has attracted considerable attention in recent years because of its relevance to a wide range of engineering applications, including biomechanics, soft robotics, aerospace structures, and flexible electronic devices [1–5]. Unlike classical linear elastic materials, hyperelastic materials exhibit highly nonlinear stress–strain behavior, which makes their mechanical response more complex and difficult to model accurately [6].

The dynamic response of hyperelastic materials has been investigated using both analytical and numerical approaches. Analytical solutions provide valuable insight into the fundamental behavior of these materials [7]. However, because large-deformation problems are inherently complex, numerical techniques particularly the finite element method (FEM) have become essential tools for their analysis [8,9]. Advances in computational mechanics have made it possible to simulate large-deformation responses with increasing accuracy, enabling the investigation of a broad range of loading scenarios and boundary conditions [10,11]. In addition, experimental studies have confirmed the occurrence of nonlinear wave phenomena in soft materials, further highlighting the need for robust and reliable modeling approaches [12,13].

Among various hyperelastic material models, the Gent model [14] is a widely accepted framework for capturing the finite deformation behavior of such materials, especially those with limited chain extensibility. This model effectively addresses the stiffening observed in polymeric and biological materials, rendering it a crucial tool for researchers in material science and structural mechanics [15,16]. A key challenge in modeling hyperelastic beams lies in selecting appropriate constitutive models. The Gent model, specifically, is frequently employed due to its capacity to incorporate the finite extensibility of polymer chains, thus offering a more realistic representation for biological and soft materials [15,17]. When contrasted with other hyperelastic models, such as the Mooney–Rivlin and Ogden models, the Gent model provides a more accurate approximation for materials subjected to extreme deformations [18].

Understanding the dynamic response of hyperelastic beams undergoing large deformations is essential for accurately predicting their performance in real-world applications. Classical beam theories are inadequate for capturing the nonlinear and time-dependent behavior inherent in hyperelastic structures [19,20]. Therefore, advanced formulations that incorporate finite elasticity and nonlinear kinematics are necessary [21]. Such approaches offer a more comprehensive understanding of the intricate interaction between material nonlinearity, large deformations, and dynamic effects; an understanding that is critical for designing and analyzing flexible medical devices and morphing aerospace structures [22–25].

Numerous studies have addressed the dynamic analysis of beam structures for various applications [26–29]. Destrade et al. [23] investigated the influence of the nonlinear characteristics of hyperelastic materials and showed that such behavior can introduce dispersion and attenuation effects in wave propagation. Using nonlocal continuum theory in conjunction with Euler–Bernoulli beam theory, Civalek and Demir [30] examined the buckling behavior of a cantilever carbon nanotube (CNT) beam. Hameury et al. [31] studied large-amplitude vibrations through an experimental setup developed for the active control of a sandwich beam.

Arefi et al. [32] analyzed the nonlinear vibration of functionally graded (FG) Timoshenko nanobeams, emphasizing the effects of flexoelectricity, surface energy, and residual stress. Alibakhshi et al. [33] investigated the nonlinear vibration of a microcantilever using the Euler–Bernoulli beam model. The dynamics of a multilayered microbeam with an axially functionally graded core and an intermediate elastic support were examined in [34], where the modal decomposition method was employed to handle the coupled equations of motion.

The dynamic instability of a sandwich beam based on the third-order shear deformation theory was comprehensively analyzed in [35]. Adela Mejia-Nava et al. [36] also investigated the instability of geometrically exact beams under both static and dynamic conditions. The deformation behavior of an Euler–Bernoulli FG nanobeam containing a crack was examined in [37]. In-plane buckling of small- and large-curvature FG microbeams was studied in [38] using the isogeometric collocation method. The coupled dynamic response of a double-beam system reinforced with functionally graded CNTs was investigated in [39].

Aria et al. [40] employed the finite element method to study the thermal vibration of a cracked nanobeam. Peng et al. [41] modeled the mechanical behavior of 3D-printed sandwich cellular structures. The dynamic analysis of porous composite beams with geometric imperfections was carried out in [42]. Karami et al. [43] applied nonlocal strain-gradient theory to examine the dynamic behavior of nanobeams in a thermal environment. Firouzi et al. [44] investigated nonlinear free vibrations of geometrically exact beams under different boundary conditions. Finally, Bayat et al. [45] presented a comprehensive review of engineering structures, including beams reinforced with carbon nanotubes and graphene platelet nanofillers.

A review of the existing literature shows that most studies on the dynamic response of beam structures have focused primarily on geometrically exact beam formulations. The aim of this study is to develop a comprehensive framework for analyzing the transient response of hyperelastic beams subjected to large deformations. Specifically, the objective is to model beams made of rubber-like hyperelastic materials whose strain-stiffening behavior at large stretches is accurately captured by the Gent model. Because the response is dynamic, inertia effects are explicitly included.

The principal nonlinearities considered in this work include material nonlinearity, represented through the Gent hyperelastic constitutive law; geometric nonlinearity, arising from finite strains and large rotations; and dynamic nonlinearity, which appears through inertia effects and nonlinear internal forces. By incorporating advanced numerical techniques, this research seeks to bridge the gap between theoretical modeling and practical applications.

In this study, the Gent hyperelastic model is adopted, the time integration is performed using the implicit Newmark method, and a nonlinear finite element formulation for a five-parameter beam element is developed. The results contribute to a deeper understanding of hyperelastic materials and their behavior in modern engineering applications.

The remainder of this paper is organized as follows. Section 2 presents the derivation of the kinematic quantities associated with finite beam deformations. Section 3 develops the constitutive equations for the Gent hyperelastic beam model. Section 4 is dedicated to the finite element formulation for large-deformation dynamic analysis of beams. Several illustrative examples are provided and solved in Section 5. Finally, Section 6 summarizes the key findings and conclusions of the study.

2 Governing Kinematical Relations for Large Deformations of a Beam

In this section, the governing kinematic relations for the finite deformation of a straight beam are derived. Two Cartesian coordinate systems $\{X_1, X_2, X_3\}$ and $\{x_1, x_2, x_3\}$ are considered: one representing the reference configuration and the other the deformed state. The reference coordinate system is initially aligned with the beam's undeformed centroidal axis. The beam has an initial length L, while its cross-section is characterized by a width b and a thickness h.

When subjected to various loading conditions, the beam undergoes deformation into its current (deformed) configuration, as illustrated in Fig. 1. This framework forms the basis for analyzing large deformations and for establishing subsequent formulations for hyperelastic beam behavior.

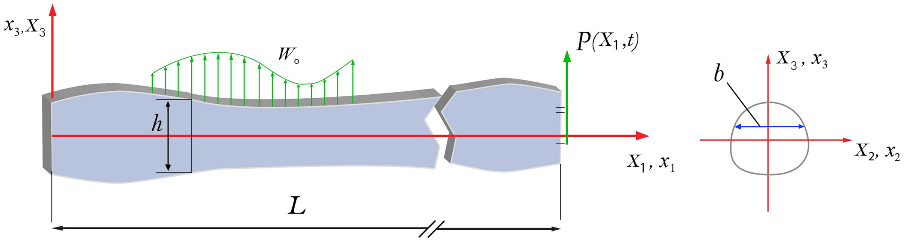

Figure 1: Schematics of a beam showing dimensions and loading conditions.

The deformation of the beam is assumed to be two-dimensional and confined to the X_1X_3-plane. Accordingly, the position of an arbitrary point within the beam can be described as

$$\mathbf{X} = X_1 \vec{\mathbf{r}}_1 + X_3 \vec{\mathbf{r}}_3, \tag{1}$$

where $\vec{\mathbf{r}}_1$ and $\vec{\mathbf{r}}_3$ denote the unit basis vectors in theX_1- andX_3-directions, respectively. After deformation, the position of the same point can be expressed as follows [46]:

$$\mathbf{x} = \mathbf{x}_0 \left(X_1, t\right) + \left(X_3 + X_3^2 \xi \left(X_1, t\right)\right) \mathbf{w} \left(X_1, t\right). \tag{2}$$

Here, ξ denotes the stretch parameter introduced to prevent the Poisson locking phenomenon, and t represents time. In addition, $\mathbf{w}$ is the director vector that characterizes the rotation of the beam cross-section. A new parameter, referred to as the difference vector, is defined as

$$\mathbf{y} = \{y_1, y_3\}^{\mathrm{T}} = \mathbf{w} - \vec{\mathbf{r}}_3. \tag{3}$$

Furthermore, by introducing the displacement vector

$$\mathbf{u} = \{u_1, u_3\}^{\mathrm{T}} = \mathbf{x}_0 - X_1\vec{\mathbf{r}}_1, \tag{4}$$

the deformation gradient tensor can then be obtained as follows:

$$\begin{aligned}\mathbf{F} = {} & \mathrm{Grad}\left(\mathbf{u}\right) + \vec{\mathbf{r}}_1 \otimes \mathrm{Grad}\left(X_1\right) + \left(\mathbf{y} + \vec{\mathbf{r}}_3\right) \\ & \otimes \mathrm{Grad}\left(X_3 + \xi X_3^2\right) + \left(X_3 + \xi X_3^2\right) \mathrm{Grad}\left(\mathbf{y}\right).\end{aligned} \tag{5}$$

The linearized form of the deformation gradient tensor can be expressed as

$$\mathbf{F} = \mathbf{F}_0 + X_3\mathbf{F}_1 + \mathcal{O}\left(X_3^2\right), \tag{6}$$

in which $\mathbf{F}_0$ and $\mathbf{F}_1$ are defined as

$$\mathbf{F}_0 = \left(1 + u'\right) \vec{\mathbf{r}}_1 \otimes \vec{\mathbf{r}}_1 + y_1\vec{\mathbf{r}}_1 \otimes \vec{\mathbf{r}}_3 + u_3'\vec{\mathbf{r}}_3 \otimes \vec{\mathbf{r}}_1 + \left(1 + y_3\right) \vec{\mathbf{r}}_3 \otimes \vec{\mathbf{r}}_3, \tag{7}$$

$$\mathbf{F}_1 = y_{1,X_1}\vec{\mathbf{r}}_1 \otimes \vec{\mathbf{r}}_1 + 2\xi y_1\vec{\mathbf{r}}_1 \otimes \vec{\mathbf{r}}_3 + y_{3,X_1}\vec{\mathbf{r}}_3 \otimes \vec{\mathbf{r}}_1 + 2\xi\left(1 + y_3\right) \vec{\mathbf{r}}_3 \otimes \vec{\mathbf{r}}_3. \tag{8}$$

Based on the deformation gradient tensor, the right Cauchy–Green deformation tensor is expressed as

$$\mathbf{C} = \mathbf{F}^{\mathrm{T}}\mathbf{F} = \mathbf{C}_0 + X_3\mathbf{C}_1. \tag{9}$$

Here, $\mathbf{C}_0$ and $\mathbf{C}_1$ are defined as follows

$$\begin{aligned}\mathbf{C}_0 = {} & \left[\left(1 + u_{1,X_1}\right)^2 + {u_{3,X_1}}^2\right]\left(\vec{\mathbf{r}}_1 \otimes \vec{\mathbf{r}}_1\right) + \left[\left(1 + u_{1,X_1}\right) y_1 + u_{3,X_1}\left(1 + y_3\right)\right] \\ & \cdot \left(\vec{\mathbf{r}}_1 \otimes \vec{\mathbf{r}}_3 + \vec{\mathbf{r}}_3 \otimes \vec{\mathbf{r}}_1\right) + \left[y_1^2 + \left(1 + y_3\right)^2\right]\left(\vec{\mathbf{r}}_3 \otimes \vec{\mathbf{r}}_3\right).\end{aligned} \tag{10}$$

$$\begin{aligned}\mathbf{C}_1 = {} & \left[2y_{1,X_1}\left(1 + u_{1,X_1}\right) + 2y_{3,X_1}u_{3,X_1}\right]\left(\vec{\mathbf{r}}_1 \otimes \vec{\mathbf{r}}_1\right) + \left[4\xi y_1^2 + 4\xi\left(1 + y_3\right)^2\right] \\ & \cdot \left(\vec{\mathbf{r}}_3 \otimes \vec{\mathbf{r}}_3\right) + \left[y_1y_{1,X_1} + y_{3,X_1}\left(1 + y_3\right) + 2\xi y_1\left(1 + u_{1,X_1}\right)\right. \\ & \left. + 2\xi\left(1 + y_3\right) u_{3,X_1}\right]\left(\vec{\mathbf{r}}_1 \otimes \vec{\mathbf{r}}_3 + \vec{\mathbf{r}}_3 \otimes \vec{\mathbf{r}}_1\right).\end{aligned} \tag{11}$$

It should be noted that the Green–St. Venant strain tensor is calculated as

$$\mathbf{E} = \mathbf{E}_0 + X_3\mathbf{E}_1 \tag{12}$$

Here, $\mathbf{E}_0$ and $\mathbf{E}_1$ are given by:

$$\begin{aligned}\vec{\mathbf{E}}_0 = {} & \frac{1}{2}\left[\left(1 + u_{1,X_1}\right)^2 + u_{3,X_1}^2 - 1\right]\vec{\mathbf{r}}_1 \otimes \vec{\mathbf{r}}_1 + \frac{1}{2}\left[y_1^2 + \left(1 + y_3\right)^2 - 1\right]\vec{\mathbf{r}}_3 \otimes \vec{\mathbf{r}}_3 \\ & + \frac{1}{2}\left[\left(1 + u_{1,X_1}\right) y_1 + u_{3,X_1}\left(1 + y_3\right)\right]\left(\vec{\mathbf{r}}_1 \otimes \vec{\mathbf{r}}_3 + \vec{\mathbf{r}}_3 \otimes \vec{\mathbf{r}}_1\right),\end{aligned} \tag{13}$$

$$\begin{aligned}\vec{\mathbf{E}}_1 = {} & \left[y_{1,X_1}\left(1+u_{1,X_1}\right) + y_{3,X_1}u_{3,X_1}\right]\vec{\mathbf{r}}_1\otimes\vec{\mathbf{r}}_1 + \left[2\xi\left(y_1^2+\left(1+y_3\right)^2\right)\right]\vec{\mathbf{r}}_3\otimes\vec{\mathbf{r}}_3 \\ & + \frac{1}{2}\left[y_{1,X_1}y_1 + y_{3,X_1}\left(1+y_3\right) + \xi\left(1+u_{1,X_1}\right)\right. \\ & \left. + \xi\left(1+y_3\right)u_{3,X_1}\right]\left(\vec{\mathbf{r}}_1\otimes\vec{\mathbf{r}}_3 + \vec{\mathbf{r}}_3\otimes\vec{\mathbf{r}}_1\right). \end{aligned} \tag{14}$$

Accordingly, the degrees of freedom for the beam element consist of the displacement parameters $\{u_1, u_3\}$, the components of the difference vector $\{y_1, y_3\}$, and the stretch parameter ξ. Therefore, five unknown variables need to be determined at each point along the beam.

3 Strain Energy Function and Stress Calculation

In this work, the Gent strain energy density function is adopted to model the finite deformation behavior of hyperelastic beams, which is expressed as follows [13]:

$$W = -\frac{1}{2}\mu J_m \ln\left[1-\frac{\left(I_{1\mathrm{C}}-2\right)}{2}\right] - \mu\ln J + c\beta^{-2}\left(\beta\ln J + J^{-\beta} - 1\right). \tag{15}$$

In this expression, $I_{1\mathrm{C}}$ is the first invariant of the Cauchy–Green strain tensor. The quantity J denotes the Jacobian of the deformation gradient tensor, that is, $J = \det\left(\mathbf{F}\right)$. In addition, μ, c and β are material parameters, where J_m represents the chain-extensibility parameter. It is also noted that as $J_m \to \infty$, the Gent model reduces to the classical neo-Hookean hyperelastic formulation.

Based on the strain energy density function, the corresponding stress measures can be derived. In large-deformation analysis, multiple stress definitions may be used depending on the formulation and requirements of the problem. In this study, the 2nd Piola–Kirchhoff stress tensor is employed, as it is energetically conjugate to the Green–Lagrange strain tensor within the Lagrangian framework. The 2nd Piola–Kirchhoff stress tensor is obtained as follows:

$$\mathbf{S} = 2W_{,\mathbf{C}} = -\frac{\mu J_m}{I_{1\mathrm{C}} - J_m - 2}\mathbf{I} - \mu\mathbf{C}^{-1} + c\beta^{-1}\left(1-2J^{-\beta}\right)\mathbf{C}^{-1}, \quad \mathbf{S} = \mathbf{S}_0 + X_3\mathbf{S}_1 \tag{16}$$

In beam structural analysis, it is customary to express quantities in a linearized form, where one component represents the in-plane deformation and the other corresponds to the curvature effects, as introduced in Eq. (1). To obtain the linear representation of the stress, several preliminary calculations are required [46]:

$$\mathbf{C}^{-1} = \mathbf{C}_0^* + X_3\mathbf{C}_1^*, \quad \text{with} \quad \mathbf{C}_0^* = \mathbf{C}_0^{-1}, \quad \mathbf{C}_1^* = -\mathbf{C}_0^{-1}\mathbf{C}_1\mathbf{C}_0^{-1}, \tag{17}$$

$$J = J_0 + X_3 J_1, \quad \text{with} \quad J_0 = \det\left(\mathbf{F}_0\right), \quad J_1 = \det\left(\mathbf{F}_1\right), \tag{18}$$

$$I_{1\mathrm{C}} = I_{10} + X_3 I_{11}, \quad \text{with} \quad I_{10} = \det\left(\mathbf{C}_0\right), \quad I_{11} = \det\left(\mathbf{C}_1\right). \tag{19}$$

The linearized form of the stress is obtained as follows:

$$\mathbf{S}_0 = -\frac{\mu J_m}{I_{10} - J_m - 2}\mathbf{I} - \mu\mathbf{C}_0^* + c\beta^{-1}\left(1 - 2\exp\left(-\beta\ln J_0\right)\right)\mathbf{C}_0^*, \tag{20}$$

$$\begin{aligned}\mathbf{S}_1 = {} & \frac{\mu J_m}{I_{10} - J_m - 2}\mathbf{I} - \mu\mathbf{C}_1^* + c\beta^{-1}\left(1 - 2\exp\left(-\beta\ln J_0\right)\right)\mathbf{C}_1^* \\ & + 2cJ_0^{-1}J_1\exp\left(-\beta\ln J_0\right)\mathbf{C}_0^*. \end{aligned} \tag{21}$$

Moreover, the elasticity tensor is obtained by differentiating the second Piola–Kirchhoff stress tensor with respect to the right Cauchy–Green tensor, leading to the following relation:

$$\begin{aligned}\mathbb{C} = {} & \frac{2\mu J_m}{\left(I_1 - J_m - 2\right)^2}\mathbf{I}\otimes\mathbf{I} - 2cJ^{-\beta}\mathbf{C}^{-1}\otimes\mathbf{C}^{-1} \\ & + \left[\mu - c\beta^{-1}\left(1 - 2J^{-\beta}\right)\right]\left(\mathbf{C}^{-1}\overline{\otimes}\mathbf{C}^{-1} + \mathbf{C}^{-1}\underline{\otimes}\mathbf{C}^{-1}\right).\end{aligned} \tag{22}$$

Here, $\overline{\otimes}$ and $\underline{\otimes}$ are the non-standard tensor product. Considering $\mathbf{Q}$ and $\mathbf{H}$ as two second-order tensors, the non-standard tensor products are defined as:

$$\left[\left(\mathbf{Q}\right)\overline{\otimes}\left(\mathbf{H}\right)\right]_{ijkl} = Q_{ik}H_{jl}, \qquad \left[\left(\mathbf{Q}\right)\underline{\otimes}\left(\mathbf{H}\right)\right]_{ijkl} = Q_{il}H_{jk}. \tag{23}$$

Representation of the fourth-order elasticity tensor in linearized form yields the following relations:

$$\begin{aligned}\mathbb{C}_0 = {} & \frac{2\mu J_m}{\left(I_{10} - J_m - 2\right)^2}\mathbf{I}\otimes\mathbf{I} + 2c\exp\left(-\beta\ln J_0\right)\mathbf{C}_0^*\otimes\mathbf{C}_0^* \\ & + \left[\mu - c\beta^{-1}\left(1 - 2\exp\left(-\beta\ln J_0\right)\right)\right]\left(\mathbf{C}_0^*\overline{\otimes}\mathbf{C}_0^* + \mathbf{C}_0^*\underline{\otimes}\mathbf{C}_0^*\right),\end{aligned} \tag{24}$$

$$\begin{aligned}\mathbb{C}_1 = {} & -\frac{4\mu J_m I_{11}}{\left(I_{10} - J_m - 2\right)^3}\mathbf{I}\otimes\mathbf{I} + 2c\exp\left(-\beta\ln J_0\right)\left(\mathbf{C}_0^*\otimes\mathbf{C}_1^* + \mathbf{C}_1^*\otimes\mathbf{C}_0^*\right) \\ & - 2c\beta J_0^{-1}J_1\exp\left(-\beta\ln J_0\right)\mathbf{C}_0^*\otimes\mathbf{C}_0^* + 2\left[\mu - c\beta^{-1}\left(1 - 2\exp\left(-\beta\ln J_0\right)\right)\right] \\ & \cdot\left(\mathbf{C}_0^*\overline{\otimes}\mathbf{C}_1^* + \mathbf{C}_1^*\overline{\otimes}\mathbf{C}_0^* + \mathbf{C}_0^*\underline{\otimes}\mathbf{C}_1^* + \mathbf{C}_1^*\underline{\otimes}\mathbf{C}_0^*\right) \\ & - 2cJ_0^{-1}J_1\exp\left(-\beta\ln J_0\right)\left(\mathbf{C}_0^*\overline{\otimes}\mathbf{C}_0^* + \mathbf{C}_0^*\underline{\otimes}\mathbf{C}_0^*\right).\end{aligned} \tag{25}$$

4 Finite Element Analysis

In this section, a nonlinear finite element formulation for the large-amplitude dynamic response of hyperelastic beams is developed. For this purpose, Hamilton's principle is expressed as follows [9]:

$$\int_{t_1}^{t_2}\delta T - \delta W^{\text{int}} + \delta W^{\text{ext}} = 0. \tag{26}$$

In this expression, δT, δW^{int}, and δW^{ext} denote the virtual kinetic energy, the virtual internal energy, and the virtual work of external forces, respectively. Within each beam element, the generalized displacement field is approximated using the following discretization:

$$\mathbf{U} = \left\{u_1, u_3, y_1, y_3, \xi\right\} = \sum_{I=1}^{\tilde{n}} N_I\left(\eta\right)\left\{u_{1I}, u_{3I}, y_{1I}, y_{3I}, \xi_I\right\}. \tag{27}$$

Here, N_I are the interpolation functions and $\tilde{n}$ is the number of nodes per element. The virtual kinetic energy is derived as follows:

$$\delta T = \int_V \rho\mathbf{U}_{,t}\cdot\delta\mathbf{U}_{,t}, \tag{28}$$

where ρ is the density. By taking integral by part, it is re-written as:

$$\delta T = -\int_V \rho\mathbf{U}_{,tt}\cdot\delta\mathbf{U}. \tag{29}$$

Using Eq. (27), the virtual kinetic energy can be evaluated as follows:

$$\delta T = -\int_L \delta \mathbf{U}^T \mathbf{m} \ddot{\mathbf{U}} d X_1, \tag{30}$$

where $\mathbf{m}$ is the element mass matrix, whose components are obtained from the following relation:

$$m_{IJ} = \int_A \rho N_I^T N_J dA, \tag{31}$$

in which A represents the initial cross-sectional area of the beam. By assembling the element mass matrices over all elements, the final expression for the virtual kinetic energy is obtained

$$\delta T = -\mathfrak{A}_{e=1}^{NE} \delta \mathbf{U}^T \mathbf{M} \ddot{\mathbf{U}}, \qquad \mathbf{M} = \int_L \mathbf{m} d X_1. \tag{32}$$

Here, $\mathfrak{A}_{e=1}^{NE}$ denotes the assembly operator. Next, the virtual work of the external loads can be written as follows:

$$\delta W^{\text{ext}} = \int_V \mathbf{f} \cdot \delta \mathbf{U} \, dV + \int_\Omega \mathbf{T} \cdot \delta \mathbf{U} \, d\Omega, \tag{33}$$

where $\mathbf{f}$ and $\mathbf{T}$ denote the body force per unit volume V and the external traction vector acting on a unit area, respectively. By neglecting the body force and assembling the external forces over all elements, the global expression for the external virtual work can be written as:

$$\delta W^{\text{ext}} = \mathfrak{A}_{e=1}^{NE} \delta \mathbf{U}^{\mathrm{T}} \mathbf{f}^{\text{ext}} = \mathfrak{A}_{e=1}^{NE} \sum_{I=1}^{\tilde{n}} \delta \mathbf{U}_I^{\mathrm{T}} \mathbf{f}_I^{\text{ext}}, \tag{34}$$

in which $\mathbf{f}_I^{\text{ext}}$ denotes the external force acting at the I'th node, given by:

$$\mathbf{f}_I^{\text{ext}} = \int_L N_I^T (X) \left\{ T_1, T_2, T_3, T_4, T_5 \right\}^T \mathrm{d} X_1. \tag{35}$$

The virtual internal energy is expressed as:

$$\delta W^{\text{int}} = \int_V \delta W (\mathbf{C}) \, \mathrm{d} V = \int_L \int_A W_{,\mathbf{C}} : \delta \mathbf{C} \, \mathrm{d} A \mathrm{d} X_1 = \int_L \int_A \mathbf{S} : \delta \mathbf{E} \, \mathrm{d} A \mathrm{d} X_1. \tag{36}$$

It should be noted that the force and moment resultants are obtained as:

$$\begin{aligned} \vec{\mathbf{F}} &= \int_A \vec{\mathbf{S}} \, \mathrm{d} A = \int_A \left(\vec{\mathbf{S}}_0 + X_3 \vec{\mathbf{S}}_1 \right) \mathrm{d} A = A \vec{\mathbf{S}}_0, \\ \vec{\mathbf{P}} &= \int_A \vec{\mathbf{S}} X_3 \mathrm{d} A = \int_A \left(\vec{\mathbf{S}}_0 + X_3 \vec{\mathbf{S}}_1 \right) X_3 \mathrm{d} A = \tilde{I} \vec{\mathbf{S}}_1. \end{aligned} \tag{37}$$

Here, $\tilde{I}$ denotes the second moment of area (area moment of inertia). Substituting Eqs. (37) into (36) yields the following relation:

$$\delta W^{\text{int}} = \int_L \left(\delta \vec{\mathbf{E}}_0^{\mathrm{T}} \vec{\mathbf{F}} + \delta \vec{\mathbf{E}}_1^{\mathrm{T}} \vec{\mathbf{P}} \right) \mathrm{d} X. \tag{38}$$

The Green-St Venant strain tensor can be approximated using the strain-displacement matrices as follows:

$$\left\{\delta\mathbf{E}_{\gamma},\Delta\mathbf{E}_{\gamma}\right\}=\sum_{I=1}^{\tilde{n}}\mathbf{B}_{\gamma I}\left\{\delta\mathbf{U},\Delta\mathbf{U}\right\},\quad\gamma=0,1,\tag{39}$$

where $\mathbf{B}_{0I}$ and $\mathbf{B}_{1I}$ denote the linear and nonlinear strain–displacement matrices, respectively. Consequently, the discretized form of the virtual internal energy is expressed as follows:

$$\delta W^{\text{int}}=\mathfrak{A}_{e=1}^{NE}\delta\mathbf{U}^{\mathrm{T}}\mathbf{f}^{\,\text{int}}=\mathfrak{A}_{e=1}^{NE}\sum_{I=1}^{\tilde{n}}\delta\mathbf{U}_{I}^{\mathrm{T}}\mathbf{f}_{I}^{\,\text{int}},\tag{40}$$

in which $\mathbf{f}_I^{\text{int}}$ is the internal force at I'th node and given by

$$\mathbf{f}_{I}^{\text{int}}=b\int_{L}\left(\mathbf{B}_{0I}^{\mathrm{T}}\vec{\mathbf{F}}+\mathbf{B}_{1I}^{\mathrm{T}}\vec{\mathbf{P}}\right)\mathrm{d}X.\tag{41}$$

Finally, by substituting Eqs. (32), (34), and (40) into the governing formulation, the following expression is obtained:

$$\mathfrak{A}_{e=1}^{NE}\delta\mathbf{U}^{\mathrm{T}}\left(-\mathbf{M}\ddot{\mathbf{U}}+\mathbf{f}^{\,\text{ext}}-\mathbf{f}^{\,\text{int}}\right)=\mathbf{0}.\tag{42}$$

As $\delta\mathbf{U}$ is not zero, it is concluded that:

$$\mathbf{M}\ddot{\mathbf{U}}+\mathbf{f}^{\,\text{int}}\left(\mathbf{U}\right)=\mathbf{f}^{\,\text{ext}}.\tag{43}$$

Several approaches have been proposed in the literature for solving the nonlinear system of Eq. (43). In the present study, the Newmark method is adopted for time discretization. Assuming that the solution is known at time step t_n, the objective is to determine the corresponding quantities at time step t_{n+1}, where $\Delta t=t_{n+1}-t_n$denotes the time increment. Accordingly, the updated expressions for displacement and velocity can be written as follows [47]:

$$\mathbf{U}_{n+1}=\mathbf{U}_{n}+\Delta t\dot{\mathbf{U}}_{n}+\Delta t^{2}\left(\frac{1}{2}-\mathrm{B}\right)+\mathrm{B}\,\Delta t^{2}\ddot{\mathbf{U}}_{n+1},\tag{44}$$

$$\dot{\mathbf{U}}_{n+1}=\dot{\mathbf{U}}_{n}+\Delta t\left(1-\Lambda\right)\ddot{\mathbf{U}}_{n}+\Lambda\Delta t^{2}\ddot{\mathbf{U}}_{n+1}.\tag{45}$$

To ensure unconditional stability of the time integration scheme, the following parameter values are adopted:

$$\mathrm{B}=0.25,\Lambda=0.5.\tag{46}$$

Eq. (43) can therefore be rewritten as follows:

$$\mathbf{M}\ddot{\mathbf{U}}_{n+1}+\mathbf{f}_{n+1}^{\,\text{int}}=\mathbf{f}_{n+1}^{\,\text{ext}}.\tag{47}$$

Eq. (47) is linearized using the Newton–Raphson method. By substituting Eqs. (34) and (40), the residual vector can be obtained as follows:

$$\mathbf{R}=\mathbf{f}^{\,\text{int}}-\mathbf{f}^{\,\text{ext}}.\tag{48}$$

By applying the Newton–Raphson method, the corresponding linearized form can be expressed as follows:

$$\delta W^{\text{int}} = \mathfrak{A}_{e=1}^{NE} \delta W_e^{\text{int}} = \mathfrak{A}_{e=1}^{NE} \sum_{I=1}^{\tilde{n}} \sum_{J=1}^{\tilde{n}} \delta \mathbf{U}_I^{\mathrm{T}} \mathbf{K}_{IJ} \Delta \mathbf{U}_J = \delta \mathbf{U}^{\mathrm{T}} \mathbf{K} \Delta \mathbf{U} \tag{49}$$

in which $\mathbf{K}_{IJ}$ denotes the element stiffness matrix, defined as:

$$\mathbf{K}_{IJ} = \mathbf{K}_{IJ}^{\text{mat}} + \mathbf{K}_{IJ}^{\text{geo}}. \tag{50}$$

5 Numerical Results

This section is devoted to evaluating the performance and accuracy of the formulations developed in the previous sections. To this end, three representative examples involving complex loading and boundary conditions are investigated. In all examples, three-node quadratic beam elements with reduced integration are employed in order to prevent shear locking.

5.1 Transient Response of a Cantilever under Distributed Load

In the first example, the dynamic response of a cantilever beam subjected to a time-dependent external load is examined. The elasticity modulus is $E = 82.74$ MPa and the Poisson's ratio is $\nu = 0.2$. The length, width and thickness of beam are $L = 25.4$ cm, $b = 2.54$ cm and $h = 2.54$ cm, respectively. Moreover, the beam density is $\rho = 10.687\ \text{kg/m}^3$ and the total time is $t_{total} = 57.3 \times 10^{-4}$ s. To apply boundary conditions, the five DOFs at the left side of the cantilever are clamped as $u_1 = u_3 = y_1 = y_3 = \xi = 0$. As shown in Fig. 2, the beam is subjected to constant pressure $W_0 = 2.85$ lb/in.

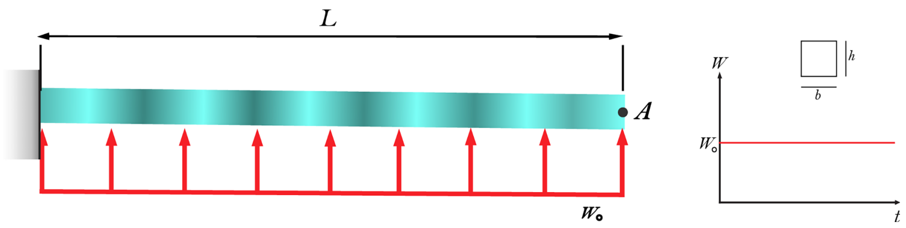

Figure 2: Schematic of cantilever subjected to distributed load.

The total simulation time is divided into increments of size $\Delta t = 1.35 \times 10^{-4}$ s. For the analysis based on the Gent model, the corresponding material parameter $\mu = 34.47$ MPa is evaluated. In addition, the parameters $\beta = -2$ and $c = 2500$ are adopted. The curves of deflection ratio u_3^A/L vs. time parameter t_p are obtained for different values of the extensibility parameter J_m and depicted in Fig. 3. The result indicates excellent agreement with the result reported by [48] when $J_m \to \infty$ in these finite element simulations, this condition is approximated by selecting a sufficiently large value for $J_m = 10^{20}$. The results demonstrate that decreasing the limiting chain extensibility parameter results in a stiffer response during the transient deformation of the hyperelastic beam. As a quantitative comparison, for example, with $J_m = 10^{20}$, the maximum nondimensional tip deflection of the beam is reduced by approximately 27% compared to the case where $J_m = 0.5$. Furthermore, the deformed configurations of the beam for $J_m = 2$ at different time parameters are illustrated in Fig. 4. In addition, a mesh sensitivity study is presented in Table 1, showing that a discretization with ten elements is sufficient to achieve accurate results.

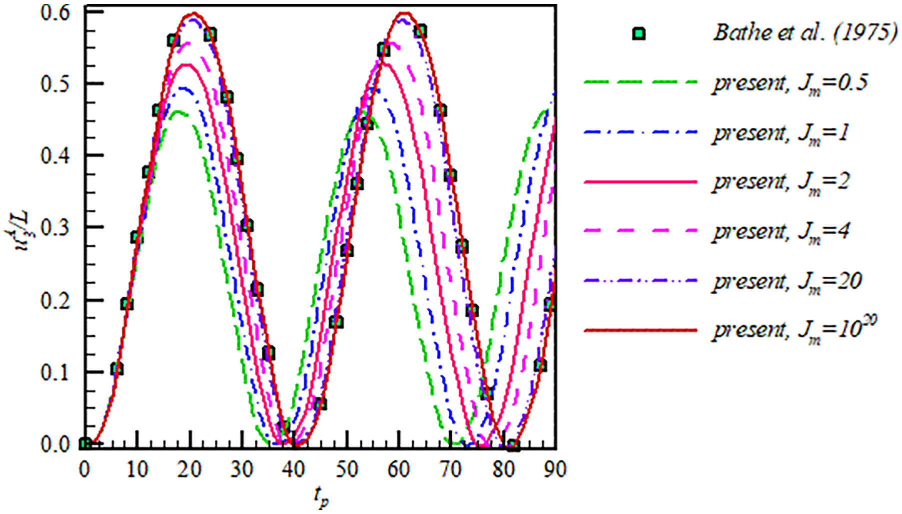

Figure 3: Time response of the nondimensional deflection u_3^A/L for different values of extensibility parameter J_m [48].

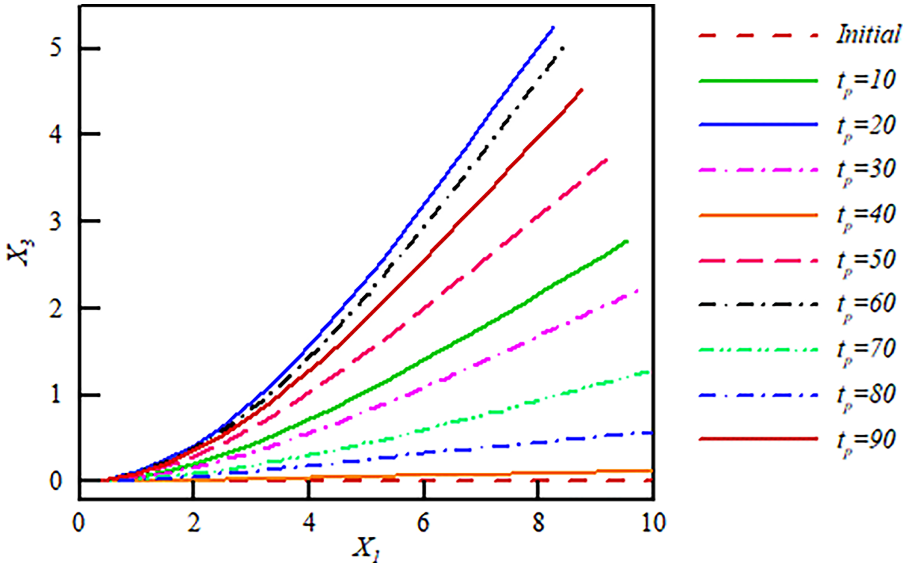

Figure 4: Deformed shapes of the cantilever at different time parameters t_p for J_m = 2.

Table 1: Mesh sensitivity analysis for dynamic response of the cantilever.

	$J_m = 0.5$	$J_m = 1$	$J_m = 2$	$J_m = 4$	$J_m = 20$	$J_m = 10^{20}$
$NE = 2$	0.9622194	0.9988941	1.0762782	1.1447489	1.2416845	1.3157287
$NE = 4$	0.9964317	1.0012000	1.0076786	1.0088675	1.0238730	1.0320543
$NE = 6$	0.9997439	1.0000901	1.0011992	1.0006999	1.0030164	1.0035884
$NE = 8$	1.0000764	1.0000013	1.0002155	1.0000818	1.0004679	1.0004123
$NE = 10$	1.0000000	1.0000000	1.0000000	1.0000000	1.0000000	1.0000000
$NE = 12$	1.0000000	1.0000000	1.0000000	1.0000000	1.0000000	1.0000000

5.2 *Dynamic Response of a Supported-Clamped Beam with One Extra Support*

In this example, the dynamic response of a clamped-supported beam, featuring an additional support at its mid-span and subjected to complex loading conditions, is investigated. The Young's modulus and the Poisson's ratio of the beam are $E = 1.4 \times 10^4$ Pa and the Poisson's ratio is $\nu = 0.3$, respectively. The density is $\rho = 10^{-4}\ \mathrm{kg/m^3}$. Besides, the length is $L = 12$ m, the width and thickness are $b = h = 1$ m. The beam is applied to a constant load $W_0 = -20$ N/m in the interval of $X_1 \in [0, 4]$ m. Moreover, it is subjected to a point load $P_1 = -6.67$ N in the $X_1 = 9$ m, as displayed in Fig. 5.

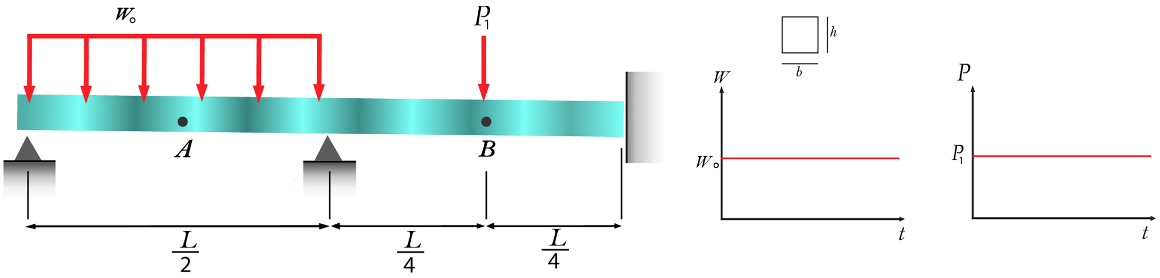

Figure 5: Schematic of supported-clamped beam with extra support in the middle subjected to distributed load at $X_1 \in [0, 4]$ m and a point load at $X_1 = 9$ m.

To impose the boundary conditions, the supported points satisfy $u_1 = u_3 = 0$, while the boundary conditions in the clamped point are $u_1 = u_3 = y_1 = y_3 = \xi = 0$. By using the Gent hyperelastic model, the material parameters are set as $\beta = -2$, $c = 4615.4$ and $\mu = 5384.6$ Pa. The curves of deflection ratio u_3^A vs. time parameter t_p are shown in Fig. 6 for different values for extensibility parameter J_m. The curves are also plotted for the location of point load and depicted in Fig. 7. The result reveals that when $J_m \to \infty$, here for finite element simulation, we consider large value $J_m = 10^{20}$. The results show that reducing the limiting chain extensibility parameter leads to a stiffer response in the transient deformation of the hyperelastic beam model. As an example, for $J_m = 10^{20}$, the maximum deflection at the point A of the beam decreases by 23% in comparison to the case where $J_m = 0.5$. Finally, the deformed configurations of the supported–clamped beam with an additional mid-span support are illustrated in Fig. 8. A mesh sensitivity analysis is also performed, and the corresponding results are summarized in Table 2.

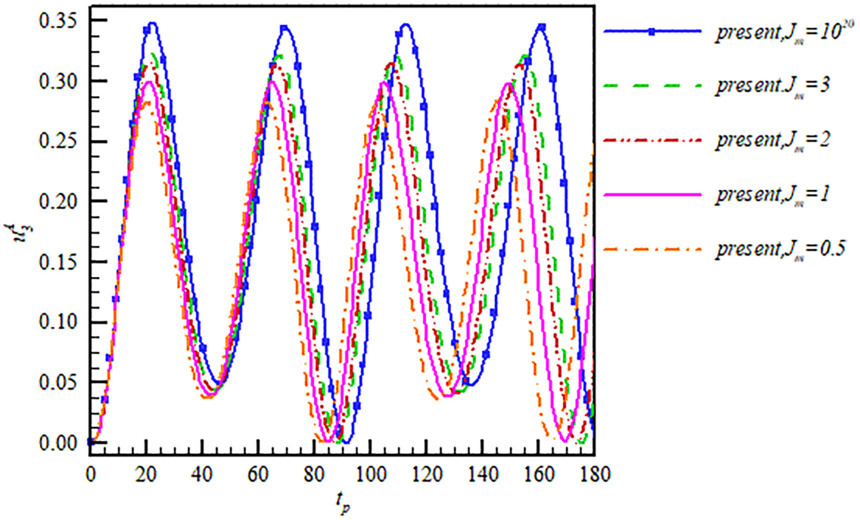

Figure 6: Time response of the deflection u_3^A for various values of J_m.

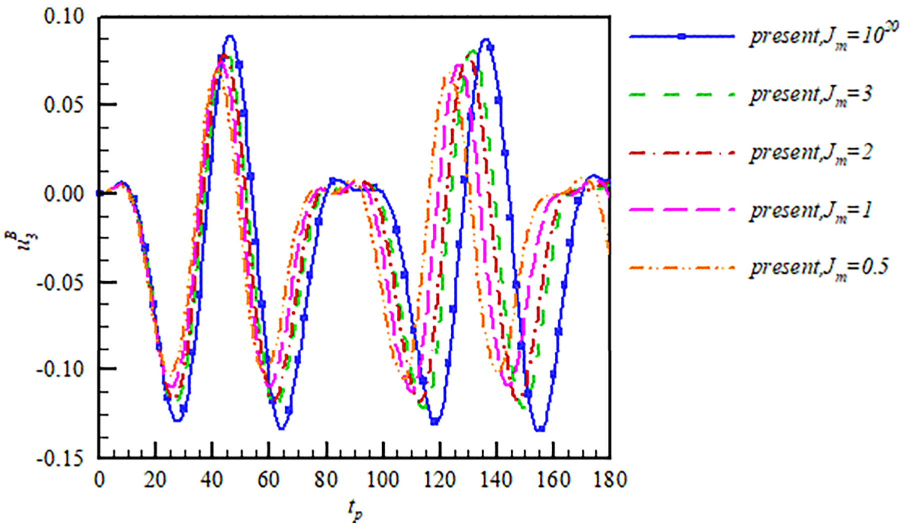

Figure 7: Time response of the deflection u_3^B for various values of parameter J_m.

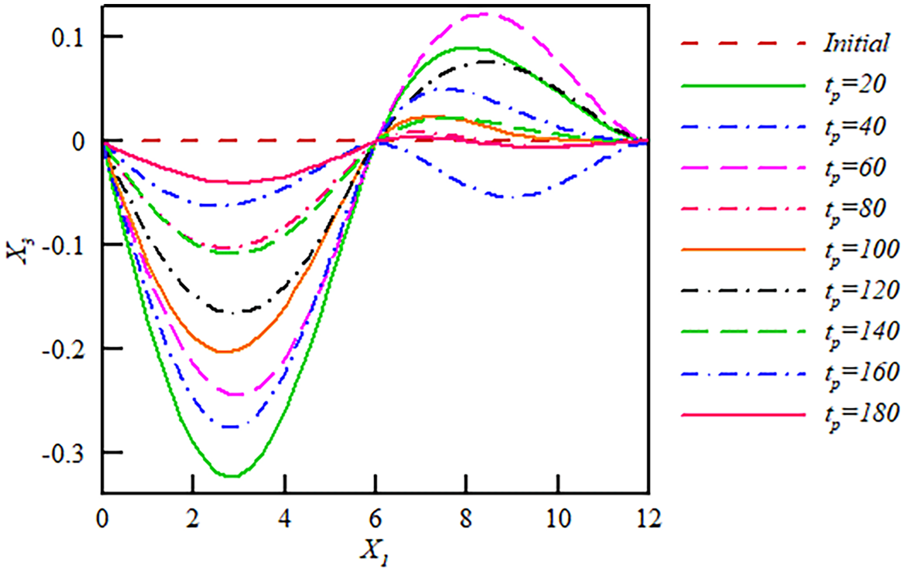

Figure 8: Deformed shapes of the supported-clamped beam with extra support in the middle at different time parameters t_p for $J_m = 3$.

Table 2: Mesh sensitivity analysis for dynamic response of the simply supported-clamped beam with one extra support.

	$J_m = 0.5$	$J_m = 1$	$J_m = 2$	$J_m = 3$	$J_m = 10^{20}$
$NE = 4$	0.8073549	0.8676084	0.8455928	0.7561741	1.7662481
$NE = 8$	0.9345453	0.9241677	0.8644630	0.7701017	1.7899937
$NE = 12$	0.9595087	0.9408307	0.8922715	0.8343928	1.8854212
$NE = 16$	0.9787287	0.9681008	0.9435270	0.9099674	1.3762555
$NE = 20$	0.9913640	0.9870096	0.9764234	0.9656469	1.1042929
$NE = 24$	1.0000000	1.0000000	1.0000000	1.0000000	1.0000000
$NE = 28$	1.0000000	1.0000000	1.0000000	1.0000000	1.0000000

5.3 Dynamic Response of a Clamped-Sliding Beam with Two Extra Supports

In the final example, the dynamic response of a clamped-sliding beam equipped with two additional supports is examined. The length of the beam is $L = 12\,\text{m}$ and one additional support is located at $X_1 = 4\,\text{m}$ and one roller is positioned at $X_1 = 8\,\text{m}$. The Young's modulus and the Poisson's ratio and the density of the beam are denoted by $E = 1.4 \times 10^4$ Pa and $\nu = 0.3$ and $\rho = 4 \times 10^{-4}\,\text{kg/m}^3$, respectively. Moreover, the width and thickness are denoted by $b = h = 1\,\text{m}$. The beam is subjected to a dead load $w_0 = -50\,\text{N/m}$ over the interval $X_1 \in [0, 4]$ m. Also, the point load $p_1 = -50\,\text{N}$ is applied at $X_1 = 6\,\text{m}$, and one point load $p_2 = -16.67\,\text{N}$ is applied at the sliding point $X_1 = L$, as illustrated in Fig. 9.

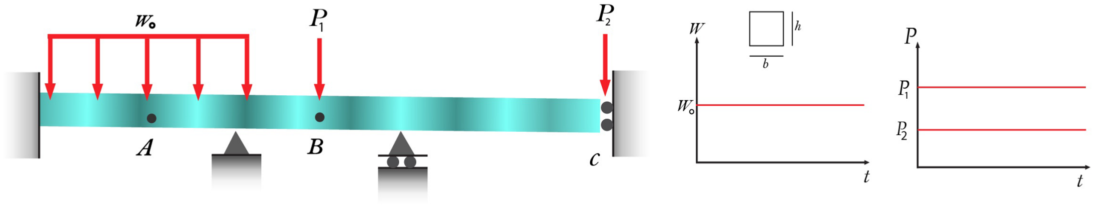

Figure 9: Schematic of clamped-sliding beam with extra support at $X_1 = 4\,\text{m}$ and roller at $X_1 = 8\,\text{m}$ subjected to distributed load at $X_1 \in [0, 4]$ m and two different point loads at $X_1 = \{6, 12\}$ m.

For this case, to enforce the boundary conditions, at the clamped end, $u_1 = u_3 = y_1 = y_3 = \xi = 0$ and the corresponding constraint must be imposed. For the left simply-supported support, the condition $u_1 = u_3 = 0$ must be imposed, while for the right support the condition, $u_3 = 0$ is applied. Moreover, for the sliding boundary at the right end of the beam, one may impose $u_1 = y_1 = y_3 = 0$. By using the Gent hyperelastic model, the material parameters are set as $\beta = -2$, $c = 4615.4$ and $\mu = 5384.6$ Pa. The deflection curves u_3^A vs. t_p are shown in Fig. 10 for different values of the extensibility parameter J_m. The curves are also plotted for the location of points B and C, and displayed in Figs. 11 and 12, respectively. The results demonstrate that when $J_m \to \infty$, here for finite element simulation, we consider a sufficiently large value of $J_m = 10^{20}$. Finally, the deformed configurations of the beam at different time steps for $J_m = 5$ are portrayed in Fig. 13.

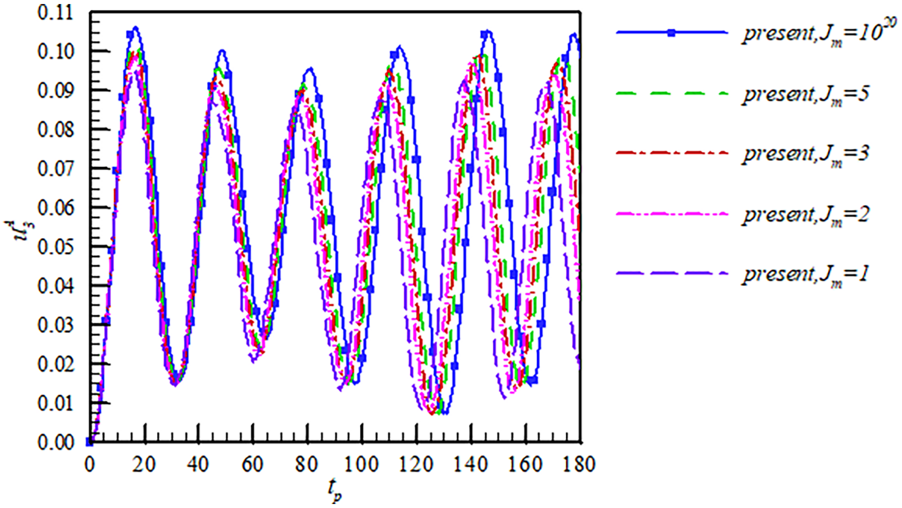

Figure 10: Time response of the deflection u_3^A in a clamped-sliding beam containing two extra supports with various values of J_m.

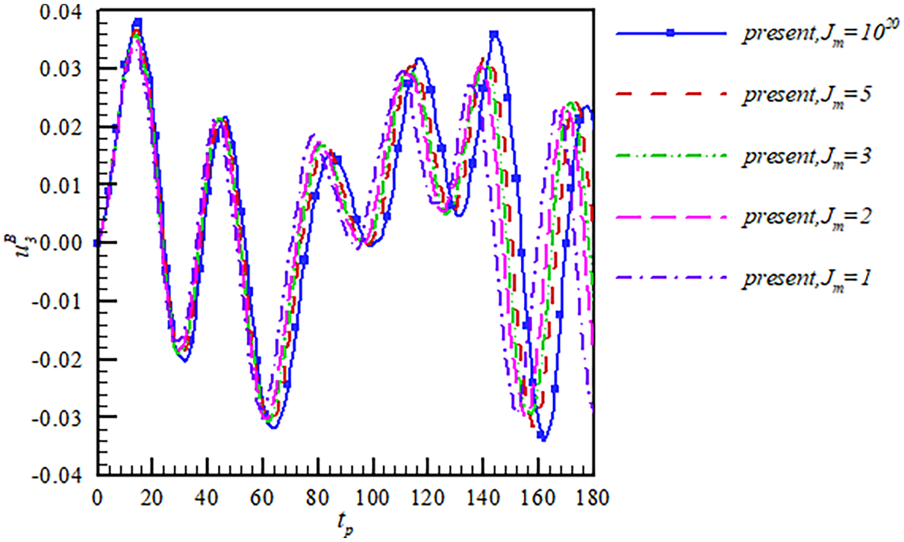

Figure 11: Time response of the deflection u_3^B in a clamped-sliding beam containing two extra supports with various values of J_m.

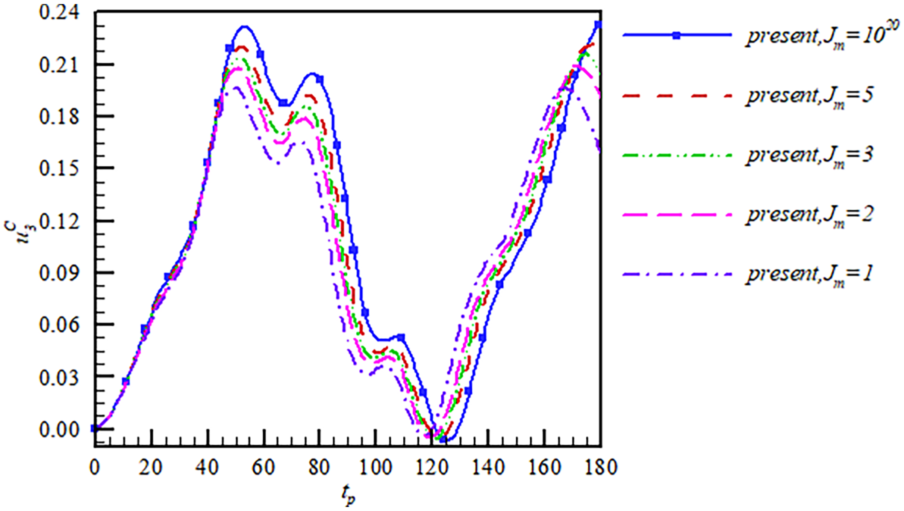

Figure 12: Time response of the deflection u_3^C in a clamped-sliding beam containing two extra supports with various values of J_m.

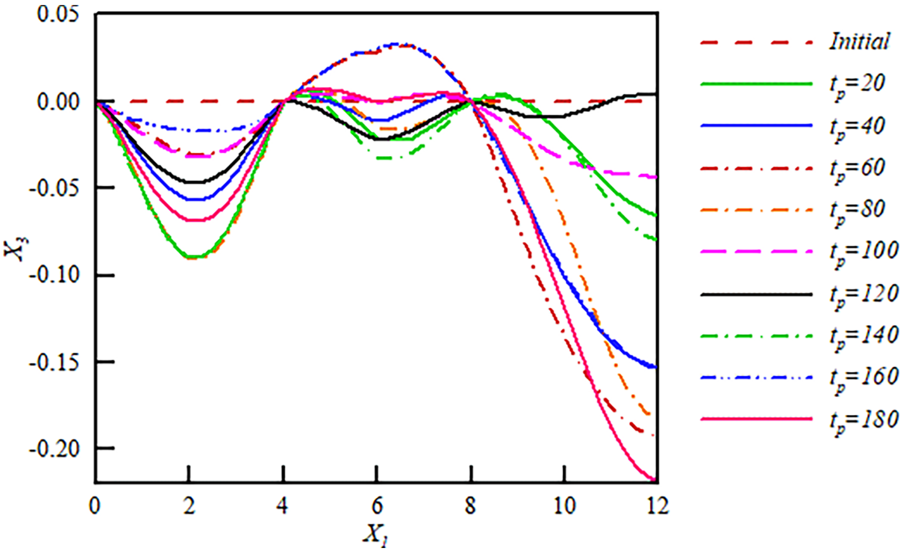

Figure 13: Deformed shapes of the supported-clamped beam with two extra supports at different time parameters t_p for $J_m = 5$.

6 Conclusion

Although the Gent hyperelastic model is well established for describing the strain-stiffening response of soft materials, its use in beam-type structural members subjected to transient dynamic loading has been only marginally explored in the existing literature. Consequently, extending this model to finite transient deformations of beams represents a meaningful and original contribution.

In this study, the Gent hyperelastic model was employed to investigate the transient response of beams under various loading scenarios and boundary conditions. The main findings can be summarized as follows:

- A formulation for the transient deformation of beam structures based on the Gent model was successfully developed.
- The finite element method enabled the analysis of beams without limitations on the applied loads or boundary constraints.
- The proposed framework consistently reduces to both the geometrically nonlinear formulation and the classical neo-Hookean model in the limit as $J_m \to \infty$.
- Incorporating chain extensibility effects leads to a stiffer structural response compared with models that neglect these effects.

Overall, the presented formulation provides a comprehensive basis for analyzing the dynamic behavior of hyperelastic beams undergoing large deformations.

Limitations and Future Developments

The present study extends the formulation of finite dynamic deformations of geometrically exact beams to the framework of the Gent hyperelastic model. Although the proposed model produces promising theoretical results, it currently remains primarily within a theoretical framework, as experimental investigations of this formulation for beam-type structures have not yet been conducted.

The Gent hyperelastic model has demonstrated strong capability in predicting the large-deformation behavior of rubber-like materials [14]. However, experimental studies focusing specifically on the dynamic response of rubber-like beam structures remain limited.

Future work may therefore focus on designing an experimental setup to investigate the dynamic behavior of rubbery beam-like structures. Such experiments would allow direct comparison between theoretical predictions and measured responses, thereby providing further validation and practical significance for the proposed model.

Acknowledgement: Not applicable.

Funding Statement: The author received no specific funding for this study.

Availability of Data and Materials: The data supporting the findings of this study are available from the corresponding author upon reasonable request.

Ethics Approval: Not applicable.

Conflicts of Interest: The author declares no conflicts of interest.

References

1. Holzapfel GA. Nonlinear solid mechanics: a continuum approach for engineering science. Chichester, UK: Wiley; 2000.
2. Ogden RW. Non-linear elastic deformations. Eng Anal. 1984;1(2):119. doi:10.1016/0264-682x(84)90061-3.
3. Dorfmann A, Ogden RW. A constitutive model for the Mullins effect with permanent set in particle-reinforced rubber. Int J Solids Struct. 2004;41(7):1855–78. doi:10.1016/j.ijsolstr.2003.11.014.
4. Ma L, Wu L, Cai CS, Li S. The theoretical impact factor spectrum for highway beam bridges. J Bridge Eng. 2021;26(12):04021089. doi:10.1061/(asce)be.1943-5592.0001800.
5. Tojaga V, Gasser TC, Kulachenko A, Östlund S, Ibrahimbegovic A. Geometrically exact beam theory with embedded strong discontinuities for the modeling of failure in structures. Part I: formulation and finite element implementation. Comput Meth Appl Mech Eng. 2023;410:116013. doi:10.1016/j.cma.2023.116013.
6. Mihai LA, Goriely A. How to characterize a nonlinear elastic material? A review on nonlinear constitutive parameters in isotropic finite elasticity. Proc R Soc A. 2017;473(2207):20170607. doi:10.1098/rspa.2017.0607.
7. Rivlin RS. Large elastic deformations of isotropic materials IV. further developments of the general theory. Philos Trans R Soc Lond Ser A Math Phys Sci. 1948;241(835):379–97. doi:10.1098/rsta.1948.0024.
8. Belytschko T, Liu WK, Moran B, Elkhodary K. Nonlinear finite elements for continua and structures. 2nd ed. Hoboken, NJ, USA: Wiley; 2013.
9. Bonet J, Wood RD. Nonlinear continuum mechanics for finite element analysis. 2nd ed. Cambridge, UK: Cambridge University Press; 2008.
10. Holzapfel GA, Gasser TC, Ogden RW. A new constitutive framework for arterial wall mechanics and a comparative study of material models. J Elast. 2000;61(1–3):1–48.
11. Reese S, Govindjee S. A theory of finite viscoelasticity and numerical aspects. Int J Solids Struct. 1998;35(26–27):3455–82. doi:10.1016/s0020-7683(97)00217-5.
12. Mihai LA, Chin L, Janmey PA, Goriely A. A comparison of hyperelastic constitutive models applicable to brain and fat tissues. J R Soc Interface. 2015;12(110):20150486. doi:10.1098/rsif.2015.0486.
13. Horgan CO, Murphy JG. Constitutive modeling for moderate deformations of slightly compressible rubber. J Rhel. 2009;53(1):153–68. doi:10.1122/1.3037263.
14. Gent AN. A new constitutive relation for rubber. Rubber Chem Technol. 1996;69(1):59–61. doi:10.5254/1.3538357.
15. Horgan CO, Saccomandi G. A description of arterial wall mechanics using limiting chain extensibility constitutive models. Biomech Model Mechanobiol. 2003;1(4):251–66. doi:10.1007/s10237-002-0022-z.

16. Beatty MF. An average-stretch full-network model for rubber elasticity. J Elast. 2003;70(1):65–86. doi:10.1023/B:ELAS.0000005553.38563.91.
17. Ogden RW, Saccomandi G, Sgura I. Fitting hyperelastic models to experimental data. Comput Mech. 2004;34(6):484–502. doi:10.1007/s00466-004-0593-y.
18. Gent AN. Elastic instabilities in rubber. Int J Non Linear Mech. 2005;40(2–3):165–75. doi:10.1016/j.ijnonlinmec.2004.05.006.
19. Love AEH. A treatise on the mathematical theory of elasticity. 4th ed. Cambridge, UK: Cambridge University Press; 1922.
20. Reddy JN. Energy principles and variational methods in applied mechanics. 2nd ed. New York, NY, USA: Wiley; 2002.
21. Antman SS. Nonlinear problems of elasticity. 2nd ed. Berlin/Heidelberg, Germany: Springer; 2005.
22. Coman CD, Bassom AP. On the wrinkling of a pre-stressed annular thin film in tension. J Mech Phys Solids. 2007;55(8):1601–17. doi:10.1016/j.jmps.2007.01.006.
23. Destrade M, Gilchrist MD, Ogden RW. Third- and fourth-order elasticities of biological soft tissues. J Acoust Soc Am. 2010;127(4):2103–6. doi:10.1121/1.3337232.
24. Zhang Q, Li S, Zhang AM, Peng Y, Zhou K. A nonlocal nonlinear stiffened shell theory with stiffeners modeled as geometrically-exact beams. Comput Meth Appl Mech Eng. 2022;397:115150. doi:10.1016/j.cma.2022.115150.
25. Ljukovac S, Ibrahimbegovic A, Husic MC. Nonlinear dynamics and control of reissner's 2D geometrically exact beam by distributed port-Hamiltonian system. Numer Meth Eng. 2025;126(16):e70103. doi:10.1002/nme.70103.
26. Alibakhshi A, Dastjerdi S, Malikan M, Eremeyev VA. Nonlinear free and forced vibrations of a hyperelastic micro/nanobeam considering strain stiffening effect. Nanomaterials. 2021;11(11):3066. doi:10.3390/nano11113066.
27. Ibrahimbegovic A, Mejia-Nava RA, Ljukovac S. Reduced model for fracture of geometrically exact planar beam: non-local variational formulation, ED-FEM approximation and operator split solution. Numer Meth Eng. 2024;125:e7369. doi:10.1002/nme.7369.
28. Nguyen-Van V, Liu J, Peng C, Zhang G, Nguyen-Xuan H, Tran P. Dynamic responses of bioinspired plastic-reinforced cementitious beams. Cem Concr Compos. 2022;133:104682. doi:10.1016/j.cemconcomp.2022.104682.
29. Penna R, Lovisi G. Surface and nonlocal effects in piezoelectric nanobeams. Eur J Mech A. 2025;113:105715. doi:10.1016/j.euromechsol.2025.105715.
30. Civalek Ö, Demir C. Buckling and bending analyses of cantilever carbon nanotubes using the Euler-Bernoulli beam theory based on non-local continuum model. Asian J Civ Eng. 2011;12:651–61.
31. Hameury C, Ferrari G, Franchini G, Amabili M. An experimental approach to multi-input multi-output nonlinear active vibration control of a clamped sandwich beam. Mech Syst Signal Process. 2024;216:111496. doi:10.1016/j.ymssp.2024.111496.
32. Arefi M, Pourjamshidian M, Ghorbanpour Arani A, Rabczuk T. Influence of flexoelectric, small-scale, surface and residual stress on the nonlinear vibration of sigmoid, exponential and power-law FG Timoshenko nano-beams. J Low Freq Noise Vib Act Control. 2019;38(1):122–42. doi:10.1177/1461348418815410.
33. Alibakhshi A, Rahmanian S, Dastjerdi S, Malikan M, Karami B, Akgöz B, et al. Hyperelastic microcantilever AFM: efficient detection mechanism based on principal parametric resonance. Nanomaterials. 2022;12(15):2598. doi:10.3390/nano12152598.
34. Sibtain M, Yee K, Ong OZS, Ghayesh MH, Amabili M. Dynamics of size-dependent multilayered shear deformable microbeams with axially functionally graded core and non-uniform mass supported by an intermediate elastic support. Eng Anal Bound Elem. 2023;146:263–83. doi:10.1016/j.enganabound.2022.10.030.
35. Asgari GR, Arabali A, Babaei M, Asemi K. Dynamic instability of sandwich beams made of isotropic core and functionally graded graphene platelets-reinforced composite face sheets. Int J Str Stab Dyn. 2022;22(8):2250092. doi:10.1142/s0219455422500924.
36. Adela Mejia-Nava R, Imamovic I, Hajdo E, Ibrahimbegovic A. Nonlinear instability problem for geometrically exact beam under conservative and non-conservative loads. Eng Struct. 2022;265:114446. doi:10.1016/j.engstruct.2022.114446.

37. Lovisi G. Application of the surface stress-driven nonlocal theory of elasticity for the study of the bending response of FG cracked nanobeams. Compos Struct. 2023;324:117549. doi:10.1016/j.compstruct.2023.117549.
38. Sahmani S, Safaei B, Rabczuk T. Nonlinear in-plane buckling of small-curved and large-curved FG porous microbeams via strain gradient-based isogeometric collocation formulations. Compos Struct. 2024;334:117969. doi:10.1016/j.compstruct.2024.117969.
39. Ong OZS, Ghayesh MH, Losic D, Amabili M. Coupled dynamics of double beams reinforced with bidirectional functionally graded carbon nanotubes. Eng Anal Bound Elem. 2022;143:263–82. doi:10.1016/j.enganabound.2022.06.023.
40. Aria AI, Friswell MI, Rabczuk T. Thermal vibration analysis of cracked nanobeams embedded in an elastic matrix using finite element analysis. Compos Struct. 2019;212:118–28. doi:10.1016/j.compstruct.2019.01.040.
41. Peng C, Fox K, Qian M, Nguyen-Xuan H, Tran P. 3D printed sandwich beams with bioinspired cores: mechanical performance and modelling. Thin Walled Struct. 2021;161:107471. doi:10.1016/j.tws.2021.107471.
42. Khaniki HB, Ghayesh MH, Hussain S, Amabili M. Effects of geometric nonlinearities on the coupled dynamics of CNT strengthened composite beams with porosity, mass and geometric imperfections. Eng Comput. 2022;38(4):3463–88. doi:10.1007/s00366-021-01474-9.
43. Karami B, Janghorban M, Rabczuk T. Dynamics of two-dimensional functionally graded tapered Timoshenko nanobeam in thermal environment using nonlocal strain gradient theory. Compos Part B Eng. 2020;182:107622. doi:10.1016/j.compositesb.2019.107622.
44. Firouzi N, Lenci S, Amabili M, Rabczuk T. Nonlinear free vibrations of Timoshenko-Ehrenfest beams using finite element analysis and direct scheme. Nonlinear Dyn. 2024;112(9):7199–213. doi:10.1007/s11071-024-09403-3.
45. Bayat MJ, Asemi K, Kalhori A, Babaei M. Plates, beams and shells reinforced by CNTs or GPLs: a review on their structural behavior and computational methods. Comput Model Eng Sci. 2025;142(2):1351–458. doi:10.32604/cmes.2025.060222.
46. Żur KK, Firouzi N, Rabczuk T, Zhuang X. Large deformation of hyperelastic modified Timoshenko-Ehrenfest beams under different types of loads. Comput Meth Appl Mech Eng. 2023;416:116368. doi:10.1016/j.cma.2023.116368.
47. Bathe K-J. Finite element procedures. London, UK: Pearson Education; 1996.
48. Bathe KJ, Ramm E, Wilson EL. Finite element formulations for large deformation dynamic analysis. Numer Meth Eng. 1975;9(2):353–86. doi:10.1002/nme.1620090207.